ECS | The Electrochemical Society
Advancing solid state & electrochemical science & technology

Design and Development of an Innovative Barrier Layer to Mitigate Crossover in Vanadium Redox Flow Batteries

View the article online for updates and enhancements.

Design and Development of an Innovative Barrier Layer to Mitigate Crossover in Vanadium Redox Flow Batteries

Marco Cecchetti,[1] Thomas Allen Ebaugh,[2] Haoran Yu,[2] Leonard Bonville,[2] Chiara Gambaro,[3] Laura Meda,[3] Radenka Maric,[2,*] Andrea Casalegno,[1] and Matteo Zago[1,*,z]

[1]Department of Energy, Politecnico di Milano, 20156 Milano, Italy
[2]Center for Clean Energy Engineering, University of Connecticut, Storrs, Connecticut 06269, United States of America
[3]Eni DR&D Renewable Energy and Environmental R&D Center, 28100, Novara, Italy

Capacity loss induced by the undesired transport of vanadium ions across the ion-exchange membrane (i.e. crossover) is one of the most critical issues associated with vanadium redox flow batteries. This work reports on the manufacturing and testing of an innovative barrier layer to mitigate crossover. The barrier layer conceptual design is described in detail in the patent application WO 2019/197917. The barrier was deposited directly onto Nafion® 212 using the Reactive Spray Deposition Technology, in which carbon-rich particles ($\sim$4–10 nm in diameter) formed in the flame were deposited simultaneously with a mixture of 1100EW Nafion® and Vulcan® XC-72R ($\sim$40 nm diameter) that was sprayed from air-assisted secondary nozzles. During cycles at fixed capacity, the presence of the barrier layer significantly reduced battery self-discharge; the average variation of battery state of charge compared to a reference cell with Nafion® 115 was reduced from 21% to 7%. Moreover, battery energy efficiency was increased by nearly 5%, indicating that the barrier layer does not significantly hinder proton transport. During cycles at 50 mA cm^{-2} with fixed cut-off voltages, the barrier layer exhibited stable operation, maintaining a coulombic efficiency around 99.4%. Additionally, the use of the barrier layer projects to a 30% reduction of stack-specific cost.

The vanadium redox flow battery (VRFB) has received significant attention in last few years as a viable energy storage technology that exploits redox reactions of four different vanadium species (V^{2+}, V^{3+}, VO^{2+} and VO_2^+) to convert electrical energy into and from chemical energy. The VRFB is a promising technology for energy storage because of its independent scalability of capacity and power, high flexibility, high efficiency, and long cycle life.[1–4] The advantages of using VRFBs over other redox flow batteries are largely due to the use of vanadium redox couples in both half-cells. Other redox flow batteries have different elemental species in each half-cell, which can cause irreversible cross-contamination between the half-cells. Furthermore, VRFB systems can achieve high energy efficiencies up to 90%. Although VRFB systems are already commercialized, and the number of installations is continuously increasing, VRFB performance is still hindered by some technological issues, among which is the capacity loss induced by the undesired transport of vanadium ions across the ion-exchange membrane.[5–10]

The electrolyte solutions in VRFBs consist of vanadium ions dissolved in sulfuric acid. These solutions, called the anolyte and the catholyte, flow from external tanks to the electrodes of the cells. During normal discharge VO_2^+ is reduced to VO^{2+} at the positive electrode, and V^{2+} is oxidized to V^{3+} at the negative electrode. During charge, the reverse reactions occur. When vanadium ions cross the membrane, the consumption of VO_2^+ and V^{2+} occurs with no current exchange between the electrodes, leading to both electrolyte imbalance and capacity loss. In the literature,[11,12] it has been demonstrated that crossover negatively affects battery performance. Pugach et al.[11] developed a new methodology to analyse VRFB losses in a commercial scale VRFB. They quantified the effect of cross-over on both voltage losses and capacity decay, revealing that during discharge at 40 mA cm^{-2}, cross-over accounts for one third of voltage losses. Trovò et al.[12] performed a detailed quantification of losses occurring in a kW-class system, highlighting that proton conductivity is more important than species permeability,

especially at high operating current density. Thus, depending on the nominal operating conditions, the choice of a suitable membrane for VRFB application involves a trade-off between low vanadium-ion permeability and high proton conductivity. Moreover, good stability in a highly corrosive environment and low fabrication costs are necessary for product development.

Nafion® membranes are widely used in VRFBs due to their high proton conductivity and good mechanical and chemical stability. However, Nafion® membranes are quite permeable to vanadium ions. This usually necessitates the adoption of thicker Nafion® membranes to limit capacity loss, which leads to increased ohmic loss and system costs.[13] Sulfonated poly(ether ether ketone) (SPEEK) and sulfonated polyimide (SPI) membranes are alternative cation exchange membranes (CEMs) that are promising because of their reduced vanadium-ion permeability; however, their low proton conductivity and poor stability hinder their usefulness with respect to Nafion®.[14] Anion exchange membranes (AEMs) are interesting alternatives, but poor chemical stability and low conductivity limit their application in VRFBs.[14,15] Amphoteric ion exchange membranes (AIEMs) combine the functional groups of both CEMs and AEMs, resulting in both low vanadium-ion permeability and good conductivity. However, the complex preparation of these membranes results in high costs.[14,16]

In the literature, significant effort has been dedicated to the modification of membranes in order to improve vanadium/proton selectivity.[17–26] Yu et al.[17] incorporated graphene oxide nanosheets into recast Nafion® membranes, obtaining a significant decrease in vanadium-ion permeability. Similarly, Su et al.[19] proposed a graphene oxide/Nafion® composite membrane with orientated GO nanosheets. Vanadium-ion crossover in these composite membranes was reduced by two orders of magnitude, but the membrane resistance increased by an unacceptable 60%. Zhang et al.[18] reduced membrane pore size with silica, obtaining higher coulombic efficiency and similar voltage efficiency when compared to the original membrane. Kim et al.[20] developed a sandwich-like structured membrane with a central layered silicate layer by a solution-casting and hot-pressing method. The silicate layer reduced the cross-over rate, but the cell voltage efficiency at 40 mA cm^{-2} was reduced by 5% compared to a Nafion® 117 standard.

In this work, we pursued a different approach, in which an additional selective layer, described in the patent application WO 2019/197917, was deposited directly onto a commercial cation exchange membrane. The selective layer, termed as a barrier, is a porous component in which pore size, tortuous path, thickness, and composition are designed to improve vanadium/proton selectivity. Since the selectivity towards vanadium ions is mainly provided by the barrier, thinner membranes can be employed in the battery, implying system-cost reduction. Moreover, the barrier is manufactured with Reactive Spray Deposition Technology (RSDT), which is a process characterized by fast deposition time, low cost, and suitability to scale-up to the industrial scale[a], implying additional cost savings.

The work is organized as follows. Experimental section firstly describes barrier layer manufacturing by RSDT and ex situ characterization by means of scanning electron microscopy (SEM) and transmission electron microscopy (TEM); then electrochemical characterization in single-cell tests is presented. Subsequently, the experimental results are discussed and the proof of concept of the barrier layer to mitigate electrolyte imbalance is demonstrated. Finally, relevant conclusions are given.

Experimental

Barrier manufacturing by RSDT.—Barriers were deposited directly onto membrane samples at the University of Connecticut using RSDT. The RSDT is a unique flame-based synthesis process that is capable of depositing a wide range of materials directly onto a variety of substrates, especially for electrochemical applications.[27–32] For barrier fabrication, carbon-rich particles ∼4--10 nm in diameter were formed in the RSDT flame and were deposited directly onto the membrane simultaneously with a mixture of 1100EW Nafion® and Vulcan® XC-72R (∼40 nm diameter) that was sprayed from air-assisted secondary nozzles (Nordson P/N: 7021604) as shown in Fig. 1.

The flame was sprayed from the RSDT nozzle, which was fed with a liquid solution of xylene (Fisher P/N: X5-20) and propane (Airgas P/N: PR CP350DPS) as the fuel and ultra-zero grade air (Airgas P/N: AI UZ300) as the oxidant. The flame was anchored at the RSDT nozzle by pilot flames fed with premixed oxygen (Airgas P/N: OX UHP 300) and methane (Airgas P/N: ME UHP300). As seen in Fig. 1, the flame was enclosed in the "primary shroud," which limited the amount of ambient air entrained. This was essential for maintaining the correct stoichiometry for the formation of the carbon-rich particles in the flame. The flame was cooled by an annulus of compressed air from a component called the "air quench." The air quench cooled the carbon-rich particles in the flame, which prevented the oxidation of the particles and limited particle growth before the particles reached the membrane. Additionally, the air quench cooled the gases in the flame sufficiently such that the membrane was not exposed to too high a temperature during the barrier fabrication. Immediately downstream from the air quench, the methanol-based mixture of Nafion® and Vulcan® (Nafion®-to-Vulcan® weight ratio of 2:1) was injected into the gas stream from the secondary nozzles in the "quench shroud." The carbon-rich particles from the flame mixed with the Nafion® and Vulcan® in the quench shroud. The air from the air quench directed this mixture onto the membrane. After the above-mentioned barrier manufacturing, the membranes were implemented in VRFB tests without further processing.

SEM and TEM analysis of barrier layer.—Plan-view images of the barrier layer were taken with SEM. SEM images are secondary electron images taken using a FEI Quanta FEG scanning electron microscope with an ETD detector in high vacuum mode. SEM samples were gold-coated to limit the effects of charging. Images were taken using high-voltage of 5 kV, spot-size 2.5, 10 mm working distance, and 3 microseconds dwell time.

Cross-sectional samples of the barrier layer were cut transverse to the plane of the membrane by potting in Spurr's resin and cutting at room temperature using a Lecia UCT ultramicrotome equipped with an ultra 45° Diatome™ diamond knife. In this work, a 150 nm thick cross-section mounted on a 50-mesh copper TEM grid was imaged. Images were taken with a Talos TEM in both brightfield (BF) and high angle annular darkfield (HAADF) imaging modes.

Electrochemical characterization.— *Cell hardware.*—The cell active area was 25 cm^2. An interdigitated graphite distributor was used at both the positive and the negative electrodes. The reference membrane without the barrier layer was Nafion® 115 (thickness 127 μm), while the barrier layer was coupled with Nafion® 212 (thickness 50 μm). Both positive and negative electrodes were Sigracet® 39AA (nominal thickness of ∼290 μm, compressed to 230 μm[33]). A pulse dampener was inserted in the hydraulic circuit to dampen flow oscillations produced by the peristaltic pump (Watson-Marlow 323Du with a 314Dw 4 roller head pump).[34,35]

In order to monitor electrolyte state of charge (SoC) during cell open circuit operation, a through-plate hydrogen reference electrode was applied close to the cell inlet main channel of both the positive and the negative electrodes. A schematic of the experimental setup is shown in Fig. 2. The local reference electrode measurement setup has been extensively described in Refs. 36, 37. It consists of a Nafion® tube salt bridge (diameter 0.64 mm) that directly connects the surface of VRFB working electrode with a 5 M sulfuric acid electrolyte solution, in which a Gaskatel HydroFlex® reversible hydrogen electrode (RHE) is immersed.

Positive and negative electrolytes were aqueous solutions of 1 M vanadium ions and 5 M sulfuric acid (Fischer Chemicals), prepared starting from vanadium (IV) sulfate oxide hydrate (Alfa Aesar) according to the procedure described in Ref. 38. In order to avoid air infiltration, the bottles containing the electrolyte were pressurized with N$_2$.

A potentiostat (Autolab PGSTAT 30® with 10 A booster module and SCAN250 module, DC potential accuracy ±0.2% f.s., DC current accuracy ±0.5% f.s.) was used to perform cycling and measure cell impedance at 50 frequencies distributed logarithmically between 100 kHz and 1 Hz.

Experimental tests.—Two different types of charge-discharge cycles were performed.[36] In both cycle types, after each charge and discharge step, the cell was kept at open circuit for 90 s in order to acquire both cell open-circuit voltage (OCV) and electrode open circuit potentials (OCP)[b] for the evaluation of battery SoC and the SoC of each electrolyte. These quantities were then used to detect and monitor electrolyte imbalance. The correlation between electrode open circuit potentials and the corresponding SoC was derived experimentally in a previous publication by the authors,[36] in which the shape of the obtained curves is consistent with Nernst's law. In particular, the negative electrode OCP at SoC 100% and 0% are −0.433 V vs RHE and −0.174 V vs RHE, respectively; while for the positive electrode, OCPs equal to 1.282 V vs RHE and 0.981 V vs RHE correspond to a SoC of 100% and 0%.

The first type of cycling test consisted of 40 cycles, in which the same capacity was imposed during charge and discharge: in this way, a variation of battery and electrolytes SoC can be caused only by vanadium cross-over. The charging step was performed with a current density of 40 mA cm^{-2} for 3750 s (charged capacity 1.04 Ah). The low value of the current density was set to permit the utilization of nearly 40% of the ideal battery capacity and to avoid the occurrence of side reactions. The discharge step was performed with a current density of 100 mA cm^{-2} in the first 25 cycles

---

[b]In open circuit, since the reaction overpotentials are null, the measured OCP vs RHE at the positive and negative electrodes corresponds to the relative electrolyte potential (i.e., SoC).
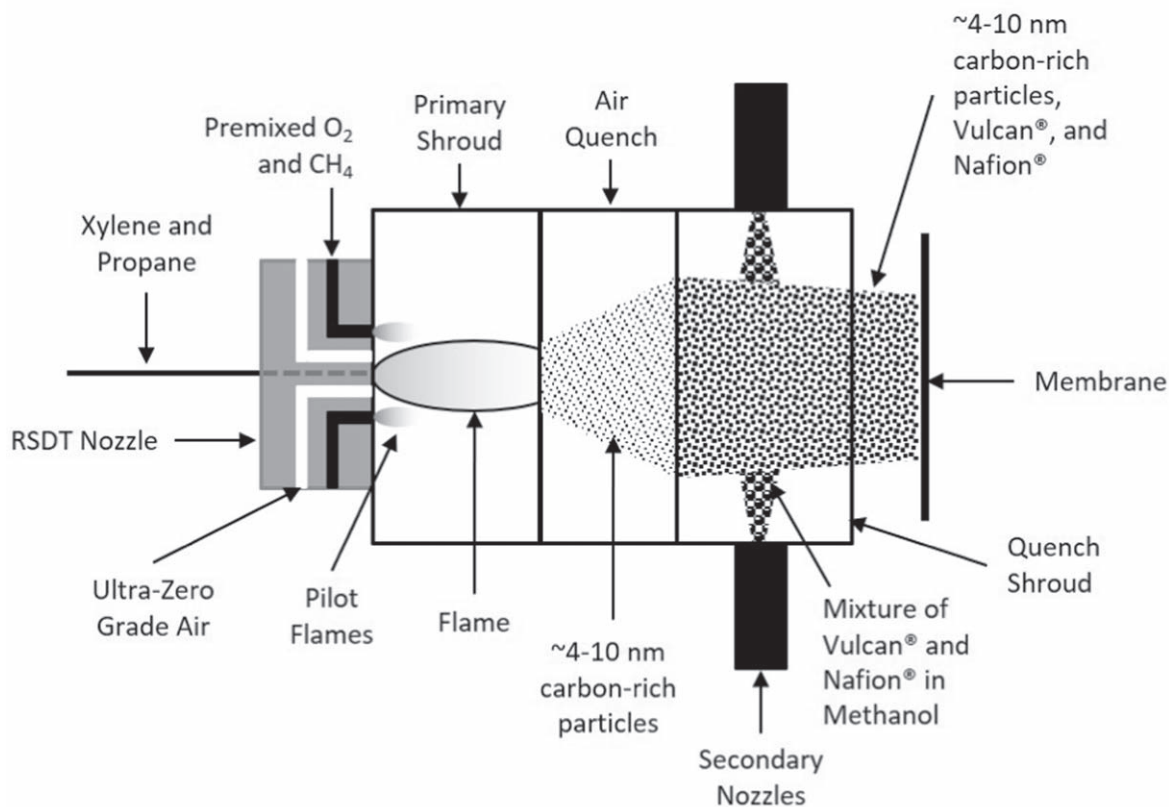
Figure 1. Diagram of the RSDT process used for depositing the barrier directly onto the membrane. Not to scale.
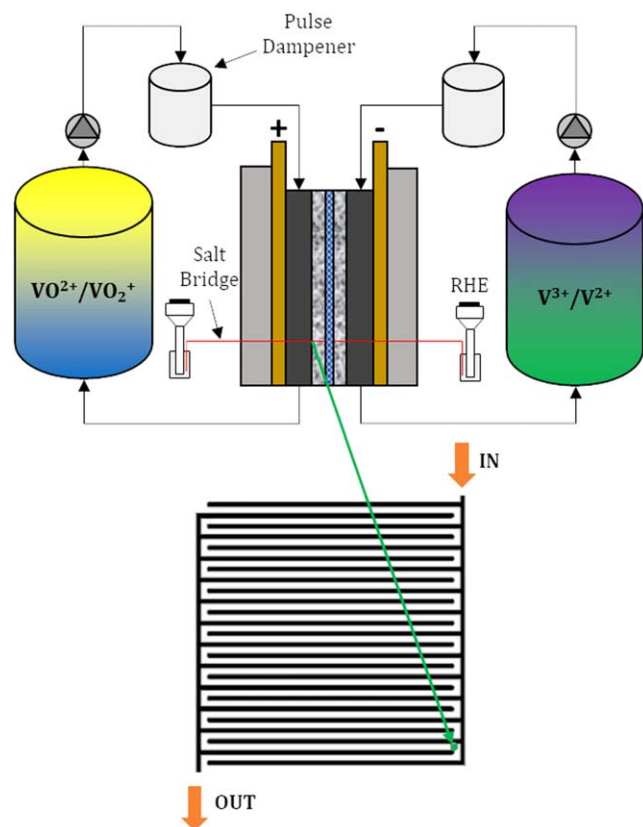

Figure 2. Schematic representation of the experimental set-up.

(discharge step duration 1500 s, discharged capacity 1.04 Ah), while the remaining 15 cycles were performed with a current density of 50 mA cm^{-2} (discharge step duration 3000 s, discharged capacity 1.04 Ah). The discharge current density was decreased after 25 cycles to tackle the continuous increase of positive and negative electrode overpotentials induced by electrolyte imbalance. The electrolyte volume during this series of cycles was 100 ml.

The second type of cycling test was used to evaluate barrier stability over time and consisted of 250 cycles at constant current (50 mA cm^{-2}), in which upper and lower voltage limits were 1.65 V and 1 V, respectively. In this type of test, voltage losses increase with cycling due to a combined effect of electrodes degradation and electrolyte imbalance induced by crossover,[27] resulting in the reduction of capacity with cycling. For this reason, at the end of the 250th cycle, electrodes were substituted with new ones to decouple the degradation effect and evaluate the impact of electrolyte imbalance on battery performance. The electrolyte volume during this series of cycles was 50 ml.

Impedance spectra were measured to determine high frequency resistance (HFR).

Results and Discussion

Ex- situ characterizations.—Figure 3 shows plan-view SEM images of the barrier layer at two different magnifications. Both images are centered at the same point. The web-like structures are likely a result of the relatively high Nafion® content in the mixture sprayed from the secondary nozzles, which has been reported by Yu et al. when spraying similar mixtures for electrodes for proton exchange membrane fuel cells.[27]

Figures 4 and 5 show TEM images of a cross-section of the barrier layer prepared by a microtome as described the experimental section. Figure 4a shows the entire thickness of the barrier layer in BF. There is a variation in the thickness throughout the image with an average thickness of approximately 2 μm. This is consistent with
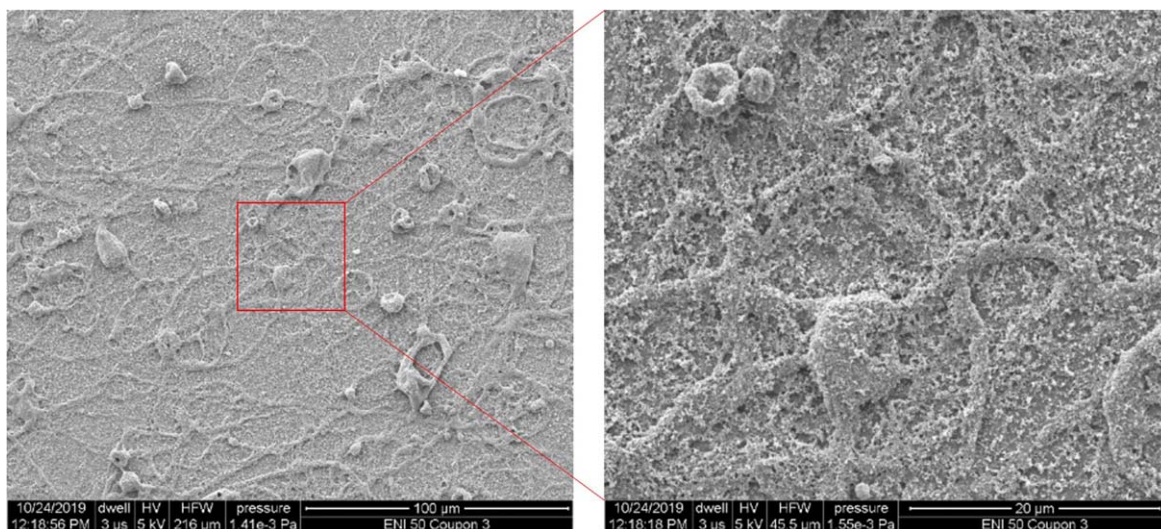
Figure 3. Representative plan-view secondary-electron SEM images of the barrier layer at different magnifications taken using a FEI Quanta FEG instrument. Both images are centred at the same point.
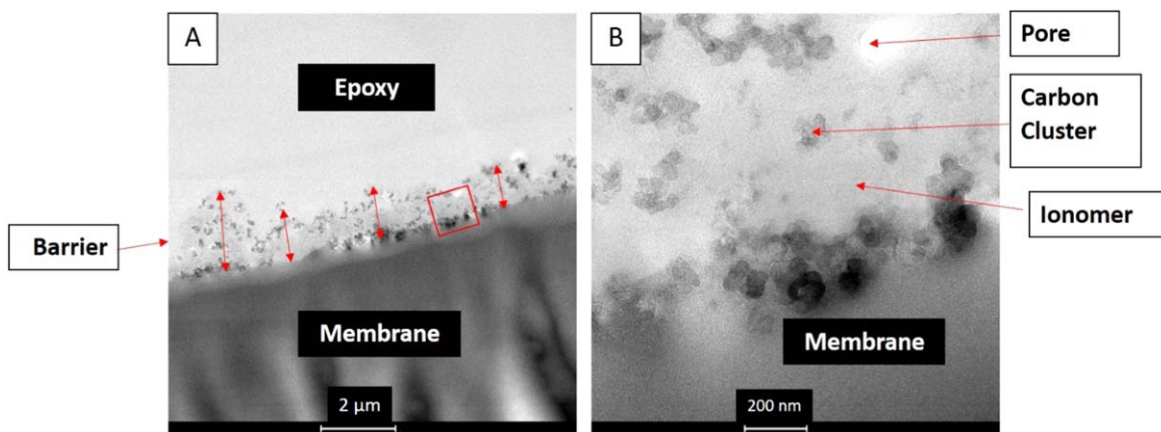

Figure 4. Bright Field TEM images of the barrier layer cross-section prepared by microtome taken using a Talos TEM: (a) low magnification showing the entire thickness of the barrier layer, which is indicated by red arrows at multiple locations along the sample; (b) higher magnification image of the barrier at a location approximated by the red box in Fig. 4a.

the cross-sectional thicknesses of many other barrier samples made to the same specifications and measured by SEM. The darker spots in the barrier layer in Fig. 4a are clusters of carbon particles. Figure 4b shows a higher magnification BF image of the selected area in Fig. 4a. Clusters of individual carbon particles can be seen. The carbon particles in most of these clusters are roughly the size of the Vulcan® particles (∼40 nm). The grey background in Fig. 4b is the Nafion® ionomer. The lighter spot toward the top-right of Fig. 4b surrounded by the grey ionomer is a closed pore approximately 100 nm in diameter in the barrier layer. This pore is not intended to influence vanadium/proton selectivity; it is an artifact of the barrier layer fabrication process. Pores that would influence vanadium/proton selectivity are ∼5 nm in diameter and are not resolved in these TEM images. This 100 nm pore is open in the direction parallel to the plane of the membrane, which is likely the result of the fact that the thickness of the cross-sectional sample cut by microtome (see experimental section) is on the same order of magnitude as the diameter of the pore. The pore is likely roughly spherical with a diameter of approximately 100 nm with this cross-section bisecting the pore. Even so, Fig. 4b shows that the pore is closed in the direction orthogonal to the plane of the membrane, which is the direction of interest for blocking vanadium crossover.

Figure 5 shows a series of HAADF images at increasing magnification clockwise from top-left at a different location from

the images in Fig. 4. In Fig. 5, the carbon features appear as bright spots. In Fig. 5a, the barrier is roughly 2 μm thick toward the middle of the image with two large bubbles filled with void space on either side. These bubbles can be associated with the surface roughness seen in the SEM images in Fig. 3. HAADF images at higher magnification are taken at the 2 μm-thick portion of the barrier layer. In Figs. 5c and 5d, it can be seen that there are carbon features of two distinct sizes. The larger carbon clusters in Fig. 5c are roughly the same size as the carbon clusters in Fig. 4b. In Fig. 5d, individual carbon particles roughly 40 nm in diameter can be seen in the larger clusters; these 40 nm particles are predominantly Vulcan®. In Figs. 5c–5d, the smaller carbon features approximately 10 nm in diameter consist of carbon-rich particles from the flame; Vulcan® does not contain 10 nm particles. The carbon-rich particles from the flame are more evident in Figs. 5c–5d than in Fig. 4b because HAADF images have stronger contrast than bright-field images. The unique barrier layer morphology achieved by the mixture of Vulcan® and carbon-rich particles from the flame creates a tortuous path for the transport of ions through the membrane, which improves vanadium/proton selectivity. The effectiveness of the barrier layer for VRFBs is demonstrated in the next section.

Electrochemical characterization.—The barrier layer has been tested at the positive and the negative sides of the cell in separate
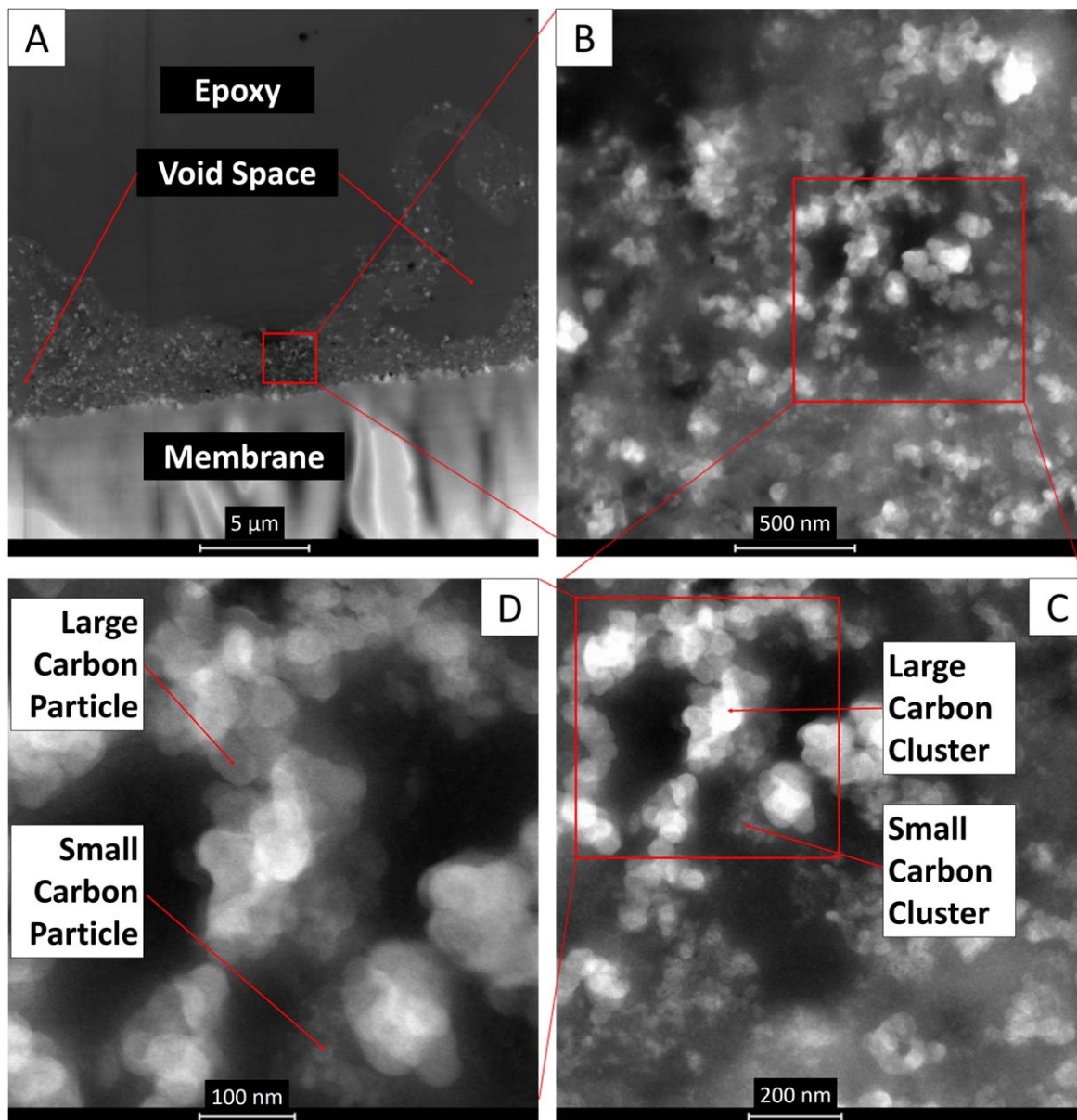
Figure 5. HAADF TEM images of the barrier layer cross-section prepared by microtome taken on a Talos TEM. Magnification increases clockwise from top-left with red boxes indicating locations of progressively higher magnifications.

tests. Figure 6 reports the results of the reference VRFB, which contains Nafion® 115, and a VRFB with the barrier at the negative side during the first type of cycle with the same capacity during the charge and discharge steps. The results of the VRFB with the barrier layer at the positive side have been omitted for the sake of figure readability; they are analogous to those with the barrier at the negative side.

Figure 6a shows the battery SoC during a typical cycle. It is worth noting that although the membrane consisting of the barrier layer and Nafion® 212 is thinner than Nafion®115, the former produces a significant reduction of battery self-discharge. This suggests that the barrier layer has significantly lower vanadium-ion permeability than bare Nafion® membranes. In particular, the average variation[c] of battery SoC between the beginning and the end of the test is 21% for the baseline cell and only 7% for the cell

with the barrier layer. Considering the electrolyte imbalance in the investigated operating conditions, the positive electrolyte undergoes higher variation of SoC (Fig. 6b) compared to the negative electrolyte (Fig. 6c). The presence of the barrier layer is effective for both electrolytes; the average variation of positive electrolyte SoC is reduced from 24% to 9%, while the average variation of negative electrolyte SoC is reduced from 16% to 5%.

The presence of the barrier layer limits electrolyte imbalance without a significant impact on membrane HFR, which slightly increases from $425 \, m\Omega \, cm^2$ to $450 \, m\Omega \, cm^2$. Despite the slightly higher HFR, the battery with the barrier layer has energy efficiency ~5% higher than the reference battery with Nafion® 115, as depicted in Fig. 6d[d]. Thus, in the investigated operating conditions, battery voltage losses are more affected by cross-over than by ohmic losses

---

[c]The average variation of battery SoC is evaluated as the average of following: the difference between the battery SoC at the end of the 1st and 40th charge steps, and the difference between the battery SoC at the end of the 1st and 40th discharge steps.

[d]The efficiency gap at cycle 25 is due to the change in current density during the discharge step, which was reduced from $100 \, mA \, cm^{-2}$ to $50 \, mA \, cm^{-2}$.
Considering the adopted cell configuration and operating conditions, $100 \, mA \, cm^{-2}$ is considered a relatively high operating current, since the resulting energy efficiency without the barrier is already lower than 80%.
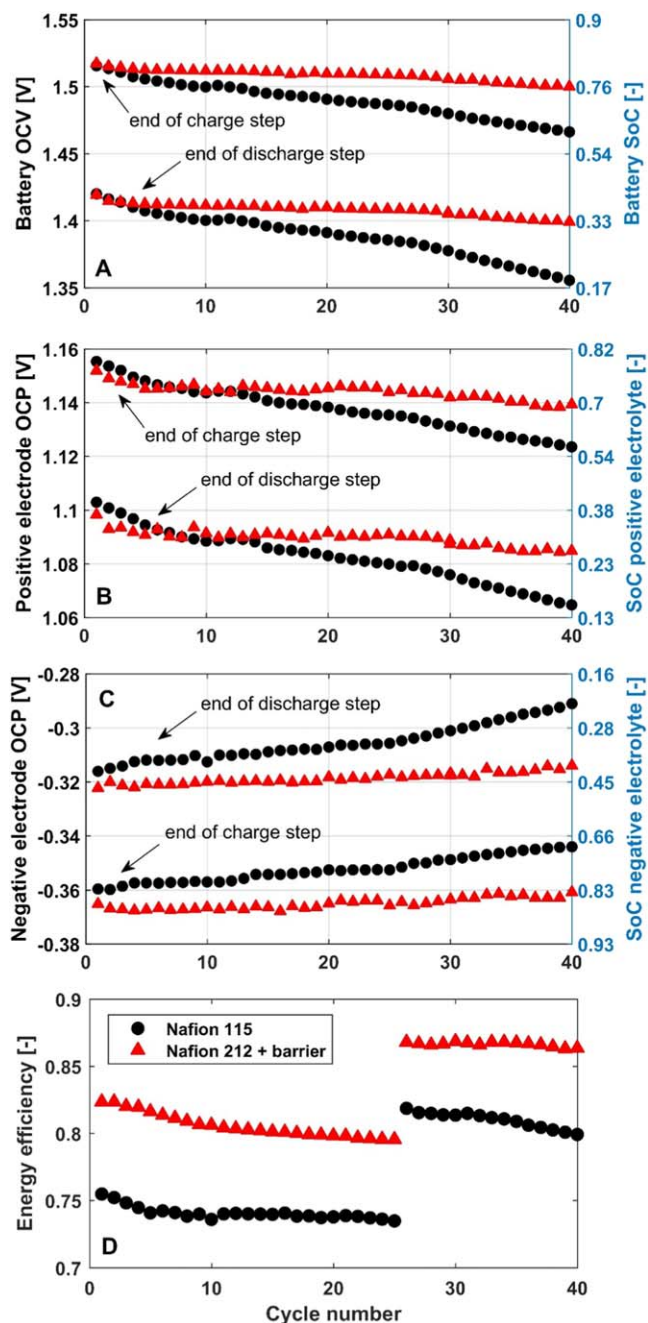
Figure 6. A typical charge/discharge cycle showing: (a) battery SoC; (b) positive electrolyte SoC; (c) negative electrolyte SoC; (d) energy efficiency.
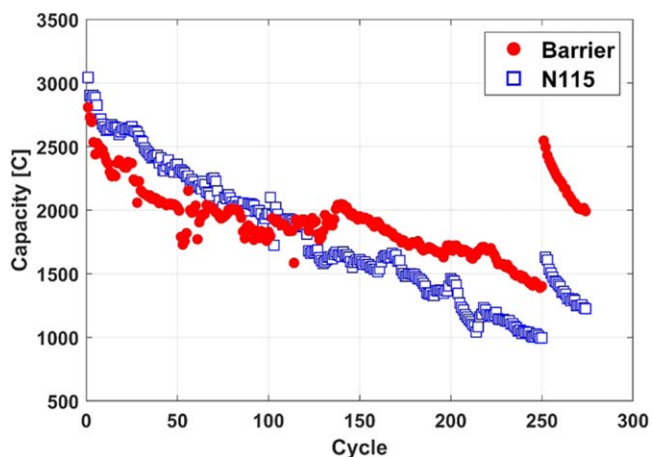

Figure 7. Evolution of discharged capacity during cycles with fixed cut-off voltages.
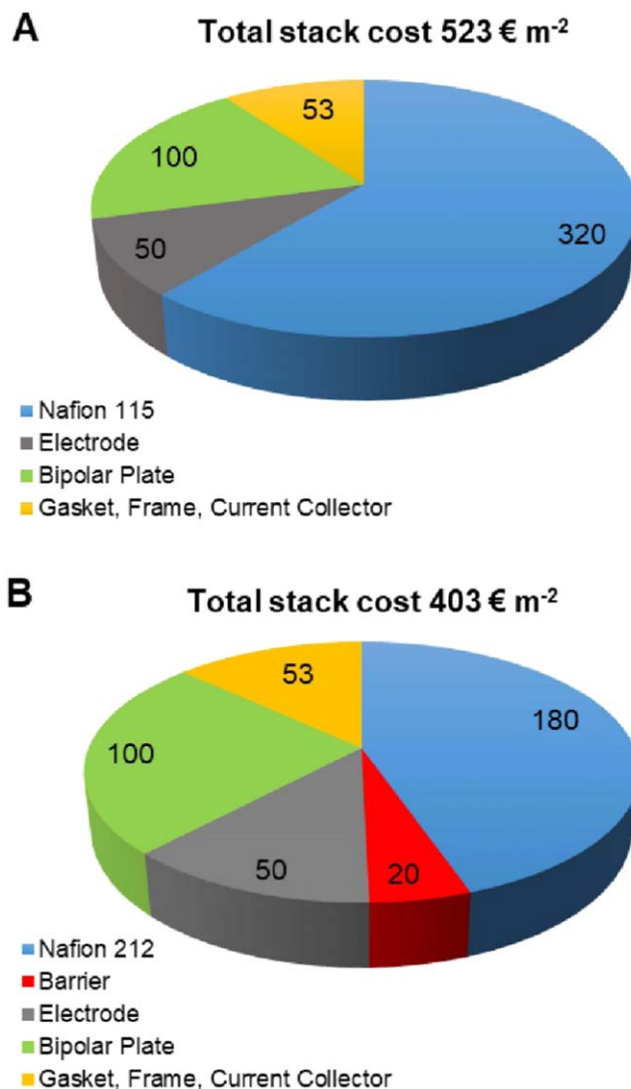
Figure 8. Stack cost breakdown: (a) VRFB with Nafion® 115; (b) VRFB with Nafion® 212 and barrier.

through the membrane.[11] The HFR associated to the barrier itself is estimated[e] to be around 200 mΩ cm^2, which results in a 1% energy efficiency loss[f]. This confirms that the impact of the barrier layer on battery voltage losses is minor.

Finally, barrier stability was evaluated during 250 cycles at 50 mA cm^{-2} with fixed cut-off voltages. Figure 7 reports the discharged capacity with both the barrier and Nafion® 115. The battery with the barrier initially exchanged a lower capacity (2809 C) because in this operating condition its energy efficiency (82% at 1st cycle) was slightly lower compared to the battery with Nafion® 115 (84% at 1st cycle). However, the coulombic efficiency of the VRFB with the barrier was higher and stable during cycling: the mean coulombic efficiency with the barrier was 99.4%, while with Nafion®

115 it was around 98.5%. This behavior resulted in a lower capacity loss with cycling for the VRFB with the barrier: at the 250th cycle the capacity loss[g] was 50% and 67% for VRFB with the barrier and

---

[e]Calculated as the difference between 450 mΩ cm^2 and the HFR of bare Nafion® 212.

[f]The efficiency loss was referred to the first cycle.

[g]Calculated with respect to the value at the 1st cycle.

Nafion® 115, respectively. As reported in Ref. 27, the capacity loss occurring in this type of cycling test results from the complex interplay between electrode degradation and electrolyte imbalance due to crossover. Thus, in order to highlight the effect of electrolyte imbalance on battery performance after 250 cycles, new electrodes were used at the 251st cycle. After the substitution of the electrodes, the exchanged capacity of the battery with the barrier was restored to 2550 C (91% of its original value), while in the case of the battery with Nafion® 115, the capacity was restored to 1650 C (54% of its original value). This result confirmed that the developed barrier was stable with cycling and was able to significantly reduce the capacity loss of the battery due to crossover.

Preliminary cost analysis.—Figure 8 reports the stack cost breakdown of a VRFB with Nafion® 115 (Fig. 8a) as the membrane and a VRFB with the barrier layer deposited on Nafion® 212 (Fig. 8b) as the membrane. The cost of Nafion® 115 and Nafion® 212 are assumed to be respectively 80% and 45%[39] of the cost of Nafion® 117, which is estimated to be 400 € m^{-2}.[40,41] The barrier layer has a manufacturing cost of approximately 20 € m^{-2}. The cost of barrier layer manufacture assumes that 75% of the fabricated material is collected on the membrane, and is estimated based on raw materials costs (Vulcan®, Nafion®, solvents, and gases) and electrical power input. The costs associated with electrodes, current collectors, and bipolar plates have been taken from Minke et al.,[42] while costs of frame and gaskets are estimated from Viswanathan et al.[43] It is worth noting that the membrane represents a significant share of the specific stack cost, as already shown in the literature.[42–45] This share of the cost can be reduced by employing a thinner membrane. Specifically, the total estimated cost of VRFB stacks using the barrier layer with Nafion® 212 is reduced by nearly 30% compared to the Nafion® 115 standard.

Conclusions

This work reports on the manufacturing and testing of an innovative barrier layer to mitigate vanadium-ion crossover in VRFBs. The concept of the barrier layer is described in the patent application WO 2019/197917. The barrier layer was deposited directly onto Nafion® 212 using the Reactive Spray Deposition Technology process. The barrier layer has an average thickness of approximately 2 μm and is composed of ionomer and carbon clusters of two distinct sizes. Larger carbon clusters are predominantly made of Vulcan® particles, while the smaller ones, approximately 10 nm in diameter, consist of carbon-rich particles from the RSDT flame.

During cycles at fixed capacity, the presence of the barrier layer significantly reduced battery self-discharge induced by crossover; the average variation of battery SoC between beginning-of-test and end-of-test was 7% with barrier layer, while without the barrier layer it was 21%. This is further confirmed by the variation of SoC of both the positive and negative electrolytes. Moreover, the barrier layer does not significantly hinder proton transport, resulting in ∼5% higher battery energy efficiency than the standard cell with Nafion® 115. During cycles at 50 mA cm^{-2} with fixed cut-off voltages, the barrier layer exhibited stable operation, maintaining a coulombic efficiency of nearly 99.4%. Additionally, the adoption of the barrier layer projects to a 30% reduction of stack specific cost compared to the Nafion® 115 standard.

The optimization of the barrier layer composition, along with the analysis of different and thinner support compared to Nafion® 212, will be performed in future work.

Acknowledgments

ORCID

Marco Cecchetti ⓘ https://orcid.org/0000-0002-5605-9920
Matteo Zago ⓘ https://orcid.org/0000-0002-0542-1459

References

1. P. Alotto, M. Guarnieri, and F. Moro, "Redox flow batteries for the storage of renewable energy: a review." *Renew. Sustain. Energy Rev.*, **29**, 325-335 (2014).
2. G. L. Soloveichik, "Flow batteries: current status and trends." *Chem. Rev.*, **115**, 11533 (2015).
3. A. Parasuraman, T. M. Lim, C. Menictas, and M. Skyllas-Kazacos, "Review of material research and development for vanadium redox flow battery applications." *Electrochim. Acta*, **101**, 27 (2013).
4. A. Z. Weber, M. M. Mench, J. P. Meyers, P. N. Ross, J. T. Gostick, and Q. Liu, "Redox flow batteries: a review." *J. Appl. Electrochem.*, **41**, 1137 (2011).
5. X. G. Yang, Q. Ye, P. Cheng, and T. S. Zhao, "Effects of the electric field on ion crossover in vanadium redox flow batteries." *Appl. Energy*, **145**, 306 (2015).
6. Y. Zhang, L. Liu, J. Xi, Z. Wu, and X. Qiu, "The benefits and limitations of electrolyte mixing in vanadium flow batteries." *Appl. Energy*, **204**, 373 (2017).
7. Y. Lei, B. W. Zhang, Z. H. Zhang, B. F. Bai, and T. S. Zhao, "An improved model of ion selective adsorption in membrane and its application in vanadium redox flow batteries." *Appl. Energy*, **215**, 591 (2018).
8. R. M. Darling, A. Z. Weber, M. C. Tucker, and M. L. Perry, "The influence of electric field on crossover in redox-flow batteries." *J. Electrochem. Soc.*, **163**, A5014 (2015).
9. T. Lagarteira, P. Pacheco, C. Almeida, A. Bentien, R. Monteiro, and A. Mendes, "In-Situ measurement of vanadium crossover for the vanadium redox flow battery." *J. Electrochem. Soc.*, **166**, A4067 (2019).
10. J. T. Vardner, J. E. Soc, J. T. Vardner, J. S. Edziah, and A. C. West, "Measurement of VO 2+ transference number in nafion with varying concentrations of sulfuric acid measurement of VO^{2+} transference number in nafion with varying concentrations of sulfuric acid." *J. Electrochem. Soc.*, **166**, A848 (2019).
11. M. Pugach, V. Vyshinsky, and A. Bischi, "Energy efficiency analysis for a kilo-watt class vanadium redox flow battery system." *Appl. Energy*, **253**, 113533 (2019).
12. A. Trovò, F. Picano, and M. Guarnieri, "Comparison of energy losses in a 9 kW vanadium redox flow battery." *J. Power Sources*, **440**, 227144 (2019).
13. B. Jiang, L. Wu, L. Yu, X. Qiu, and J. Xi, "A comparative study of Nafion series membranes for vanadium redox flow batteries." *J. Memb. Sci.*, **510**, 18 (2016).
14. Y. Shi, C. Eze, B. Xiong, W. He, H. Zhang, T. M. Lim, A. Ukil, and J. Zhao, "Recent development of membrane for vanadium redox flow battery applications: a review." *Appl. Energy*, **238**, 202 (2019).
15. L. Zeng, T. S. Zhao, L. Wei, H. R. Jiang, and M. C. Wu, "Anion exchange membranes for aqueous acid-based redox flow batteries: current status and challenges." *Appl. Energy.*, **233–234**, 622 (2019).
16. J. Dai, Y. Dong, P. Gao, J. Ren, C. Yu, H. Hu, Y. Zhu, and X. Teng, "A sandwiched bipolar membrane for all vanadium redox flow battery with high coulombic efficiency." *Polymer (Guildf).*, **140**, 233 (2018).
17. L. Yu, F. Lin, L. Xu, and J. Xi, "A recast Nafion/graphene oxide composite membrane for advanced vanadium redox flow batteries." *RSC Adv.*, **6**, 3756 (2016).
18. H. Zhang, H. Zhang, X. Li, Z. Mai, and W. Wei, "Silica modified nanofiltration membranes with improved selectivity for redox flow battery application." *Energy Environ. Sci.*, **5**, 6299 (2012).
19. L. Su, D. Zhang, S. Peng, X. Wu, Y. Luo, and G. He, "Orientated graphene oxide/Nafion ultra-thin layer coated composite membranes for vanadium redox flow battery." *Int. J. Hydrogen Energy*, **42**, 21806 (2017).
20. J. Kim, J. D. Jeon, and S. Y. Kwak, "Nafion-based composite membrane with a permselective layered silicate layer for vanadium redox flow battery." *Electrochem. Commun.*, **38**, 68 (2014).
21. C. Wu, S. Lu, J. Zhang, and Y. Xiang, "Inducing microstructural changes in Nafion by incorporating graphitic carbon nitride to enhance the vanadium-blocking effect." *Phys. Chem. Chem. Phys.*, **20**, 7694 (2018).
22. S. S. Sha'rani, E. Abouzari-Lotf, M. M. Nasef, A. Ahmad, T. M. Ting, and R. R. Ali, "Improving the redox flow battery performance of low-cost thin polyelectrolyte membranes by layer-by-Layer Surface assembly." *J. Power Sources*, **413**, 182 (2019).
23. W. Dai, Y. Shen, Z. Li, L. Yu, J. Xi, and X. Qiu, "SPEEK/Graphene oxide nanocomposite membranes with superior cyclability for highly efficient vanadium redox flow battery." *J. Mater. Chem. A.*, **2**, 12423 (2014).
24. C. Jia, Y. Cheng, X. Ling, G. Wei, J. Liu, and C. Yan, "Sulfonated poly(Ether Ether Ketone)/functionalized carbon nanotube composite membrane for vanadium redox flow battery applications." *Electrochim. Acta*, **153**, 44 (2015).
25. J. Xi, Z. Wu, X. Teng, Y. Zhao, L. Chen, and X. Qiu, "Self-assembled polyelectrolyte multilayer modified Nafion membrane with suppressed vanadium ion crossover for vanadium redox flow batteries." *J. Mater. Chem.*, **18**, 1232 (2008).
26. X. Wei, Z. Nie, Q. Luo, B. Li, B. Chen, K. Simmons, V. Sprenkle, and W. Wang, "Nanoporous polytetrafluoroethylene/silica composite separator as a high-performance all-vanadium redox flow battery membrane." *Adv. Energy Mater.*, **3**, 1215 (2013).
27. H. Yu, J. M. Roller, W. E. Mustain, and R. Maric, "Influence of the ionomer/carbon ratio for low-Pt loading catalyst layer prepared by reactive spray deposition technology." *J. Power Sources*, **283**, 84 (2015).

28. H. Yu, A. Baricci, A. Bisello, A. Casalegno, L. Guetaz, L. Bonville, and R. Maric, "Strategies to mitigate Pt dissolution in low Pt loading proton exchange membrane fuel cell: I. A gradient Pt particle size design." *Electrochim. Acta*, **247**, 1155 (2017).
29. H. Yu, A. Baricci, A. Casalegno, L. Guetaz, L. Bonville, and R. Maric, "Strategies to mitigate Pt dissolution in low Pt loading proton exchange membrane fuel cell: II. A gradient Pt loading design." *Electrochim. Acta*, **247**, 1169 (2017).
30. H. Yu, E. S. Davydova, U. Ash, H. A. Miller, L. Bonville, D. R. Dekel, and R. Maric, "Palladium-ceria nanocatalyst for hydrogen oxidation in alkaline media: optimization of the Pd–CeO 2 interface." *Nano Energy.*, **57**, 820 (2019).
31. R. Jain, Y. Lei, and R. Maric, "Ultra-low NO2 detection by gamma WO3 synthesized by reactive spray deposition technology." *Sensors Actuators, B Chem.*, **236**, 163 (2016).
32. R. Maric, J. Roller, and R. Neagu, "Flame-based technologies and reactive spray deposition technology for lowerature solid oxide fuel cells: technical and economic aspects." *J. Therm. Spray Technol.*, **20**, 696 (2011).
33. P. C. Ghimire, A. Bhattarai, R. Schweiss, G. G. Scherer, N. Wai, and Q. Yan, "A comprehensive study of electrode compression effects in all vanadium redox flow batteries including locally resolved measurements." *Appl. Energy*, **230**, 974 (2018).
34. A. M. Pezeshki, R. L. Sacci, F. M. Delnick, D. S. Aaron, and M. M. Mench, "Elucidating effects of cell architecture, electrode material, and solution composition on overpotentials in redox flow batteries." *Electrochim. Acta*, **229**, 261 (2017).
35. M. Zago and A. Casalegno, "Physically-based impedance modeling of the negative electrode in All-Vanadium Redox flow batteries: insight into mass transport issues." *Electrochim. Acta*, **248**, 505 (2017).
36. M. Cecchetti, A. Casalegno, and M. Zago, "Local potential measurement through reference electrodes in vanadium redox flow batteries: evaluation of overpotentials and electrolytes imbalance." *J. Power Sources*, **400**, 218 (2018).
37. M. Cecchetti, M. Messaggi, A. Donazzi, A. Facibeni, V. Russo, C. S. Casari, A. L. Bassi, A. Casalegno, and M. Zago, "Electrochimica Acta A combined morphological and electrochemical characterization of carbon electrodes in vanadium redox flow batteries: insights into positive and negative electrode performance." *Electrochim. Acta*, **329**, 135143 (2020).
38. D. S. Aaron, Q. Liu, Z. Tang, G. M. Grim, A. B. Papandrew, A. Turhan, T. A. Zawodzinski, and M. M. Mench, "Dramatic performance gains in vanadium redox flow batteries through modified cell architecture." *J. Power Sources*, **206**, 450 (2012).
39. A. Crawford, V. Viswanathan, D. Stephenson, W. Wang, E. Thomsen, D. Reed, B. Li, P. Balducci, M. Kintner-meyer, and V. Sprenkle, "Comparative analysis for various redox flow batteries chemistries using a cost performance model." *J. Power Sources*, **293**, 388 (2015).
40. C. Minke and T. Turek, "Materials, system designs and modelling approaches in techno-economic assessment of all-vanadium redox flow batteries—a review." *J. Power Sources*, **376**, 66 (2018).
41. M. Skyllas-Kazacos, "Performance improvements and cost considerations of the vanadium redox flow battery." *ECS Trans.*, **89**, 29 (2020).
42. C. Minke and M. A. Dorantes Ledesma, "Impact of cell design and maintenance strategy on life cycle costs of vanadium redox flow batteries." *J. Energy Storage.*, **21**, 571 (2019).
43. V. Viswanathan et al., "Cost and performance model for redox flow batteries." *J. Power Sources*, **247**, 1040 (2014).
44. S. Kim et al., "1 kW/1 kWh advanced vanadium redox flow battery utilizing mixed acid electrolytes." *J. Power Sources*, **237**, 300 (2013).
45. C. Minke, U. Kunz, and T. Turek, "Techno-economic assessment of novel vanadium redox flow batteries with large-area cells." *J. Power Sources*, **361**, 105 (2017).